JOURNAL OF PROPULSION AND POWER
Vol. 9, No. 2, March–April 1993

Multiblock Implicit Total Variation Diminishing Solution of High-Speed Internal Flows

F. Grasso* and M. Marini†
Università di Roma "La Sapienza," Rome, Italy

In this article a multiblock finite-volume technique with a second-order total variation diminishing spatial discretization and an efficient implicit time integration has been developed to simulate complex internal flows at high Mach numbers. This method employs a lower and upper approximate factorization of the implicit operator with symmetric successive over relaxation sweeps. In the presence of multiblocks, an asynchronous-interface treatment has been devised for an accurate coupling of the blocks. A detailed validation by comparison of the computed results with experiments has shown the capabilities of the method to resolve complex high-speed internal flows and to simulate the influence of bleed as a boundary-layer control system.

Nomenclature

A, B = inviscid Jacobian matrices
a = eigenvalue of inviscid Jacobian matrix
c = speed of sound
E = total energy per unit volume
e = internal energy per unit volume
$\boldsymbol{F}$ = vector flux
g = antidiffusive flux
H = total enthalpy per unit volume
I = unit tensor
k = spectral radius of viscous Jacobian matrix
L, U = lower and upper operators
N = scalar diagonal matrix
n = unit normal to cell face
P, Q = viscous Jacobian matrices
Pr = Prandtl number
p = pressure
q = heat flux
$\boldsymbol{R}$ = right eigenvector of inviscid Jacobian matrix
Re = Reynolds number
r_A, r_B = scaling parameters of spectral radii
S = cell area
T = temperature
$\boldsymbol{u}$ = velocity vector
u, v = cartesian velocities in the x and y directions, respectively
$\boldsymbol{W}$ = vector of conserved variables
x, y = cartesian coordinates
$\boldsymbol{\alpha}$ = vector of characteristic variables
γ = characteristic speed of the antidiffusive flux
Δs = cell face length
η = implicit weighting factor
μ = viscosity coefficient
ρ = density
ρ_A, ρ_B = spectral radii of inviscid Jacobian matrices
σ = stress tensor
Φ = numerical antidiffusive flux contribution
ψ = entropy function
ω = relaxation parameter

Subscripts
E = inviscid contribution
I, J = cell vertex indexes
i, j = cell indexes
num = numerical counterpart
V = viscous contribution
β = cell face index
∞ = freestream

Superscripts
e = inviscid
k = vector component
n = time level
v = viscous
0 = stagnation

Introduction

THE successful development of the second generation of supersonic transport aircrafts (SST) and of hypersonic air-breathing vehicles depends on the propulsion system and its integration with the airframe. An important role is played by fluid dynamic performances of the inlet when flying at high speed: the inlet must supply a uniform mass flow with some prescribed values of pressure, temperature, and velocity to the combustion chamber, and a given value of pressure recovery.

Flows through inlets are dominated by complex phenomena and must be optimized over the entire flight envelope. For a realistic simulation, shock-shock, shock-expansion, and shock-wave boundary-layer interactions must be accounted for. Strong viscous-inviscid interactions, typical of high Mach number flows, produce substantial modifications of the flow structure: separation and recirculation regions, with upstream propagation of disturbances through the boundary layer, and laminar-turbulent transition.

Off-design operation of fixed inlet geometries is physically possible only if flow spillage is allowed. Moreover, to make the shock system stable and avoid the unstart induced by the shock-wave boundary-layer interaction, a boundary-layer control system must be introduced as a means to enlarge the effective section of the flow.

These phenomena can be correctly predicted only by solving the complete Navier-Stokes equations, whose solution requires a strong computational effort in terms of CPU time, storage capacity, etc. In recent years, several investigators have analyzed the flows through supersonic and hypersonic inlets. Knight[1] made numerical simulations of realistic high speed inlets by solving the Navier-Stokes equations and using a flow geometry divided into overlapping regions. Garnero[2]

Received Jan. 2, 1992; revision received June 9, 1992; accepted for publication June 16, 1992.

*Associate Professor, Dipartimento di Meccanica e Aeronautica. Member AIAA.
†Ph.D. Student, Dipartimento di Meccanica e Aeronautica.

applied the multiblock technique to compute ramjet and scramjet inlet flows; Fujimoto et al.[3] have simulated the flow through supersonic inlets and the effects of bleed and throat bypass systems, by solving the Navier-Stokes equations by means of a finite-volume formulation coupled with a second-order accurate (MUSCL) scheme.

In the present work, the unsteady Navier-Stokes equations are solved for the analysis of inlet flows. An implicit lower and upper (LU) finite-volume multiblock total variation diminishing approach is developed. Yoon and Jameson[4] have first applied the LU scheme to solve transonic and supersonic flows for the Euler equations cast in a finite-volume formulation. They also developed a modified LU scheme, called LU-SSOR, that uses a symmetric successive over relaxation technique, by splitting the inviscid flux Jacobians in such a way to increase the diagonal dominance of the LU factors, and to avoid matrix inversion. Lately, Rieger and Jameson[5] extended the LU-SSOR scheme to three dimensions to solve the steady compressible Navier-Stokes equations in the framework of a finite-volume discretization technique. Grasso and Marini[6,7] have developed a lower and upper factorization scheme that uses a total variation diminishing approximation to solve complex hypersonic flows. Here the technique has been extended to a multiblock approach, that is the most qualified for realistic inlet flow simulations. The multiblock approach consists of partitioning the computational domain into regions—called blocks—so that 1) the topology of each block is rather simple; 2) the grid for each block can be easily generated; and 3) complex phenomena such as spillage, bleed, inviscid-viscous interactions, etc. can be efficiently accounted for. The partitioning of the computational domain in blocks introduces interfaces, whose treatment plays a critical role, especially in the presence of discontinuities crossing the interfaces. Spurious oscillations and distortion of shocks at interfaces have been inhibited by a conservative treatment, amounting to enforce variables continuity.

Supersonic and hypersonic inlet flows have been computed to test the validity of the implicit finite-volume multiblock approach. The computed results are compared with available numerical and experimental data, and show that the method is well-suited to predict complex inlet flows.

Governing Equations

The governing equations solved are the compressible unsteady Navier-Stokes equations in conservation form

$$\frac{\mathrm{d}}{\mathrm{d}t}\int_S \boldsymbol{W}\,\mathrm{d}S = -\oint_{\partial S}(\boldsymbol{F}_E - \boldsymbol{F}_V)\cdot n\,\mathrm{d}s \tag{1}$$

where $\boldsymbol{W}$, $\boldsymbol{F}_E$, and $\boldsymbol{F}_V$ are, respectively, the vector unknown, and the inviscid and viscous fluxes, defined as

$$\boldsymbol{W} = (\rho, \rho\boldsymbol{u}, \rho E)^T \tag{2}$$

$$\boldsymbol{F}_E = [\rho\boldsymbol{u}, \rho\boldsymbol{u}\boldsymbol{u} + p\boldsymbol{I}, \rho\boldsymbol{u}\,(E + p/\rho)]^T \tag{3}$$

$$\boldsymbol{F}_V = [0, \sigma, -(q - \boldsymbol{u}\cdot\sigma)]^T \tag{4}$$

$$\sigma = \mu(\nabla\boldsymbol{u} + \nabla\boldsymbol{u}^T) - \tfrac{2}{3}\mu\nabla\cdot\boldsymbol{u}\boldsymbol{I} \tag{5}$$

$$q = -\gamma\frac{\mu}{Pr}\nabla e \tag{6}$$

$$\mu - \mu_t = \begin{cases} \mu_\infty\tilde{T} & \text{if} \quad \tilde{T} \le s_1 \\ \mu_\infty(s_1\tilde{T})^{1/2}\dfrac{1 + s_2/s_1}{1 + s_2/\tilde{T}} & \text{if} \quad \tilde{T} > s_1 \end{cases} \tag{7}$$

where $\tilde{T} = T/T_\infty$; $s_1 = 120/T_\infty$; $s_2 = 110/T_\infty$. The turbulent viscosity μ_t is defined according to the algebraic turbulence model of Baldwin and Lomax.[8]

Numerical Solution

Realistic inlets are geometrically complex to allow proper compression of the flow. Moreover, the design of the inlets is such that the compression may be of a mixed type, both external and internal. Consequently, for an accurate modeling of the flow, one must account for spillage, bleed (necessary to have off-design operations with a fixed inlet geometry), and proper treatment of complex geometries. Therefore, a solver for simulating flows through inlets should have either block or unstructured capabilities.

At the present stage, the performance of block-structured approaches is better than the unstructured ones. For this reason, in the present work a multiblock approach has been developed together with a high-resolution implicit scheme.

For two-dimensional inlet flow simulations, the use of only two blocks is sufficient to account both for spillage and bleed. The two blocks are classified as external and internal, and for each block the computational grid is generated independently. The two meshes are equally spaced in the x direction, and stretched in the y direction. In particular, for an accurate resolution of the shock-wave boundary-layer interaction, the near wall cells must be highly stretched with a rather smooth aspect ratio distribution.[6,7]

Finite-Volume Formulation

Space and time discretizations are separated by using the method of lines, and a system of ordinary differential equations is obtained for every computational cell. A cell-centered finite-volume formulation is employed and, approximating surface and boundary integrals by means of the mean value theorem and midpoint rule, the governing equations are cast in the following discretized form[6,7]:

$$S_{i,j}\frac{\mathrm{d}\boldsymbol{W}_{i,j}}{\mathrm{d}t} + \sum_{\beta=1}^{4}(\boldsymbol{F}_{\mathrm{num}}\cdot n\Delta s)_\beta = 0 \tag{8}$$

where β stands for the generic cell face, n is the positive unit normal to cell face whose length is Δs, and $S_{i,j}$ is the cell area. The numerical flux vector is

$$\boldsymbol{F}_{\mathrm{num}} = \boldsymbol{F}_{E,\mathrm{num}} - \boldsymbol{F}_{V,\mathrm{num}} \tag{9}$$

Numerical Inviscid Flux Discretization

An upwind-biased second-order TVD scheme has been used to evaluate the inviscid flux contribution. The scheme has good properties of monotonicity and conservation in the presence of discontinuities, and it yields second-order accuracy and oscillation-free solutions (strictly true for a one-dimensional scalar equation). Thus, enforcing consistency at cell face $i + \frac{1}{2}, j$, one has

$$(\boldsymbol{F}_{E,\mathrm{num}}\cdot n\Delta s)_{i+1/2,j} = [\tfrac{1}{2}(\boldsymbol{F}_{Ei,j} + \boldsymbol{F}_{Ei+1,j})\cdot n + \Phi_{i+1/2,j}]\Delta s_{i+1/2,j} \tag{10}$$

The term $\Phi_{i+1/2,j}$ represents the numerical antidiffusive flux contribution that modifies the inviscid flux to make the scheme upwind-biased TVD and second-order accurate. Its expression is obtained by characteristic decomposition in the direction normal to cell face, thus obtaining[9,10]:

$$\Phi_{i+1/2} = \frac{1}{2}\sum_{k=1}^{4}[\psi(a^k_{i+1/2})(g^k_i + g^k_{i+1}) - \psi(a^k_{i+1/2} + \gamma^k_{i+1/2})\alpha^k_{i+1/2}]\boldsymbol{R}^k_{i+1/2} \tag{11}$$

where the subscript j has been dropped for simplicity, and $\boldsymbol{R}^k_{i+1/2}$ is the kth eigenvector.

Let U and V be, respectively, the velocity components normal and tangential to cell face. The right eigenvector matrix

of the normal inviscid flux Jacobian is[11]

$$\boldsymbol{R}_{i+1/2} = \begin{bmatrix} 1 & 1 & 1 & 0 \\ u - c\cos\theta & u & u + c\cos\theta & -\sin\theta \\ v - c\sin\theta & v & v + c\sin\theta & \cos\theta \\ H - Uc & (u^2 + v^2)/2 & H + Uc & V \end{bmatrix}_{i+1/2}$$

where $\cos\theta$, $\sin\theta$ are the components of the unit normal, and Roe's averaging is used to evaluate u, v, c, H at $i + \frac{1}{2}$.

The vector $\boldsymbol{\alpha}_{i+1/2}$ is the difference of the characteristic variables, defined as

$$\boldsymbol{\alpha}_{i+1/2} = \boldsymbol{R}^{-1}_{i+1/2}\Delta_{i+1/2}\boldsymbol{W} \tag{12}$$

The entropy function ψ here adopted is that of Harten[9]

$$\psi(z) = \begin{cases} \frac{1}{2}[(z^2/\delta) + \delta] & \text{if} \quad z < \delta \\ |z| & \text{if} \quad z \geq \delta \end{cases} \tag{13}$$

where δ is a parameter that enforces the entropy condition for vanishing eigenvalues, whose value depends on the type of flow to be computed.

g makes the scheme second-order accurate. In the present work a minmod flux limiter is employed

$$g^k_i = \text{minmod}(\alpha^k_{i-1/2}, \alpha^k_{i+1/2}) \tag{14}$$

where

$$\text{minmod}(x, y) = \text{sgn}(x)\cdot\max\{0, \min[|x|, y\cdot\text{sgn}(x)]\}$$

The characteristic speed γ^k of the antidiffusive flux is given by

$$\gamma^k_{i+1/2} = \psi(a^k_{i+1/2}) \begin{cases} \dfrac{g^k_{i+1} - g^k_i}{\alpha^k_{i+1/2}} & \text{if} \quad \alpha^k_{i+1/2} \neq 0 \\ 0 & \text{if} \quad \alpha^k_{i+1/2} = 0 \end{cases} \tag{15}$$

For second-order accuracy, boundary conditions on g are required. At all boundaries the normal derivative of g has been set equal to zero. Conservation is enforced by imposing that for all cells along the walls, the contribution (due to the modified flux Φ) in the direction normal to the wall is zero. In the presence of bleed the TVD property is enforced by imposing a nonzero contribution of the antidiffusive flux Φ through the bleed passages.

Numerical Viscous Flux Discretization

According to the constitutive equations, the viscous fluxes depend upon the gradients of the unknown vector, and the numerical counterpart is obtained by applying Gauss' theorem to a computational cell whose vertices are the two grid nodes (I, J) and $(I, J - 1)$ and the centers of the two adjacent cells (i, j) and $(i + 1, j)$. For an arbitrary function φ the numerical derivatives at $i + \frac{1}{2}, j$ are evaluated according to the following formula:

$$\left(\frac{\partial\varphi}{\partial x}\right)_{i+1/2,j} = \frac{\Delta_i\varphi\Delta_j y - \Delta_j\varphi\Delta_i y}{\Delta_i x\Delta_j y - \Delta_j x\Delta_i y}$$

$$\left(\frac{\partial\varphi}{\partial y}\right)_{i+1/2,j} = -\frac{\Delta_i\varphi\Delta_j x - \Delta_j\varphi\Delta_i x}{\Delta_i x\Delta_j y - \Delta_j x\Delta_i y}$$

where

$$\Delta_i(\cdot) = (\cdot)_{i+1,j} - (\cdot)_{i,j}; \qquad \Delta_j(\cdot) = (\cdot)_{I,J} - (\cdot)_{I,J-1}$$

The grid values $\varphi_{I,J}$, $\varphi_{I,J-1}$ are obtained by bilinear interpolation of cell center values. Hence, the discretized viscous flux contribution at cell face $i + \frac{1}{2}, j$ is an algebraic function of grid and cell center values, i.e.

$$(\boldsymbol{F}_{V,\text{num}})_{i+1/2,j} = f(\boldsymbol{W}_{i,j};\ \boldsymbol{W}_{i+1,j};\ \boldsymbol{W}_{I,J};\ \boldsymbol{W}_{I,J-1}) \tag{16}$$

Implicit Solver

Linearization of the flux vectors about the previous time step yields the unfactored implicit form of the equations[6,7]

$$S_{i,j}\frac{\Delta\boldsymbol{W}_{i,j}}{\Delta t} + \eta\sum_{\beta=1,3}[(A + P)\Delta s\Delta\boldsymbol{W}]_\beta + \eta\sum_{\beta=2,4}[(B + Q)\Delta s\Delta\boldsymbol{W}]_\beta = \boldsymbol{R}^n_{i,j} \tag{17}$$

where $\boldsymbol{R}^n_{i,j}$ is the residual, $\Delta\boldsymbol{W}_\beta$ is the time variation of the solution at cell face β, and η is a weighting factor that weighs the numerical flux between the time levels n and $n + 1$. The matrices A (B) and P (Q) are the Jacobians of the inviscid and viscous fluxes in the direction normal to cell faces $i \pm \frac{1}{2}, j$ $(i, j \pm \frac{1}{2})$:

$$A = \frac{\partial}{\partial\boldsymbol{W}}(\boldsymbol{F}_E\cdot n)_{i\pm1/2,j}; \qquad P = \frac{\partial}{\partial\boldsymbol{W}}(\boldsymbol{F}_V\cdot n)_{i\pm1/2,j}$$

A block triangular form of the implicit operator is obtained as follows. First, using flux difference concepts, the contribution of the inviscid flux Jacobians at each cell face is split into the positive and negative part. The positive (negative) inviscid flux Jacobian matrix A^+ (A^-) is constructed so that it has nonnegative (nonpositive) eigenvalues. To obtain a well-conditioned diagonally dominant operator matrix, the following formulas[4-7] have been used:

$$A^\pm = \omega^e[(A \pm \rho_A I)/2] \tag{18}$$

$$\rho_A = r_A\max(|\lambda(A)|) \tag{19}$$

where $\lambda(A)$ are the eigenvalues of the inviscid flux Jacobian, r_A is a constant of 0 (1) that affects the stability and convergence, ω^e is a relaxation parameter that enhances the effects of the inviscid eigenvalues (a value of ω^e equal to 2 has been used). Then, at cell face $i + \frac{1}{2}, j$ one has

$$(A\Delta\boldsymbol{W})_{i+1/2,j} = A^+_{i,j}\Delta\boldsymbol{W}_{i,j} + A^-_{i+1,j}\Delta\boldsymbol{W}_{i+1,j} \tag{20}$$

The viscous flux Jacobians are reduced to a diagonal form by using the spectral radii,[5-7] thus obtaining

$$P = \omega^v k_x n_x I \tag{21}$$

where k_x is the spectral radius of the viscous Jacobian matrix and ω^v is a relaxation parameter introduced to inhibit the effects of the viscous eigenvalues (a value of ω^v equal to $\frac{1}{2}$ has been used). The matrices B and Q are similarly defined.

To reduce the computational effort, a symmetric successive over relaxation technique is implemented,[4-7] therefore eliminating the need for 4×4 matrix inversion at each cell. Substituting Eqs. (18–21) and neglecting the variations of Δs_β in the x and y directions (strictly valid only for undistorted cells), the following scalar diagonal matrix is obtained:

$$N = [1 + \alpha(\rho_A\Delta s_{1,3} + \rho_B\Delta s_{2,4})]I \tag{22}$$

where

$$\alpha = \eta(\Delta t/S)_{i,j}; \qquad \Delta s_{l,m} = [(\Delta s_l + \Delta s_m)/2]$$

Then, Eq. (17) is reduced to the following factorized form:

$$L \cdot U\Delta \boldsymbol{W}_{i,j} = \beta N \boldsymbol{R}_{i,j} \tag{23}$$

where $\beta = (\Delta t/S)_{i,j}$, and L, U are the lower and upper factors. For steady-state solutions, the efficiency of the method has been improved by freezing the evaluation of the Jacobian matrices for $0(m)$ cycles. Numerical experiments[6,7] indicate that the higher the Mach number is, the more often the Jacobian matrices need to be evaluated: for supersonic flows m is 0(10); for hypersonic flows m is 0(2).

The solution of Eq. (23) is obtained in three phases.

Forward Sweep

Once the residual $\boldsymbol{R}_{i,j}$ is calculated at time level n, the forward sweep is performed

$$L\Delta \boldsymbol{W}^*_{i,j} = \beta N \boldsymbol{R}^n_{i,j} \tag{24}$$

Equation (24) is inverted performing a cell by cell sweep in the forward direction, starting from the bottom left-most corner, thus yielding at each cell i, j

$$\Delta \boldsymbol{W}^*_{i,j} = N^{-1}(N\boldsymbol{R}^n_{i,j} + \alpha A^+_{i-1,j}\Delta s_3 \Delta \boldsymbol{W}^*_{i-1,j} + \alpha B^+_{i,j-1}\Delta s_4 \Delta \boldsymbol{W}^*_{i,j-1}) \tag{25}$$

At the left and bottom boundaries $\Delta \boldsymbol{W}^*$ is set equal to zero.

Backward Sweep

Once $\Delta \boldsymbol{W}^*_{i,j}$ is obtained, the domain is swept in the backward direction (starting from the top right-most corner) and the time change of the solution is obtained according to the following equation:

$$U\Delta \boldsymbol{W}_{i,j} = \Delta \boldsymbol{W}^*_{i,j} \tag{26}$$

By matrix inversion of Eq. (26) one has

$$\Delta \boldsymbol{W}_{i,j} = N^{-1}(\boldsymbol{W}^*_{i,j} - \alpha A^-_{i+1,j}\Delta s_1 \Delta \boldsymbol{W}_{i+1,j} - \alpha B^-_{i,j+1}\Delta s_2 \Delta \boldsymbol{W}_{i,j+1}) \tag{27}$$

At the top and right boundaries $\Delta \boldsymbol{W}$ is set equal to zero.

Updating of the Solution

Once $\Delta \boldsymbol{W}_{i,j}$ is computed, the solution is updated as follows:

$$\boldsymbol{W}^{n+1}_{i,j} = \boldsymbol{W}^n_{i,j} + \Delta \boldsymbol{W}_{i,j} \tag{28}$$

Multiblock Technique

For an efficient treatment of the boundary conditions, fictitious cells are introduced along the boundaries, and the blocks are overlaid. To properly couple the blocks at the interfaces, the continuity of the variables must be imposed. In the present work, grid and metric continuities are enforced when generating the blocks, and the introduction of a fictitious layer of cells surrounding the blocks allows to impose the interface boundary conditions by injecting the solution of the underlaying block onto the overlaying one (see Fig. 1).

Two different approaches have been analyzed for the block interface treatment: 1) synchronous and 2) asynchronous.

The synchronous-interface approach amounts to solve sequentially the two blocks with an implicit interface treatment. Referring to Fig. 2, the solution of block 1 is computed first (phases L.1 and U.1). Then, the solution is injected onto block 2 at the interface (phase I.12). Finally, block 2 is updated by performing the two sweeps (phases L.2 and U.2), and the auxiliary cells of block 1 are updated by injecting the block 2 solution (phase I.21). Referring to Fig. 2, to start the forward sweep on block 2, the block matrix $B^+_{i,1}$ of Eq. (25), is required. Likewise, to start the backward sweep on block

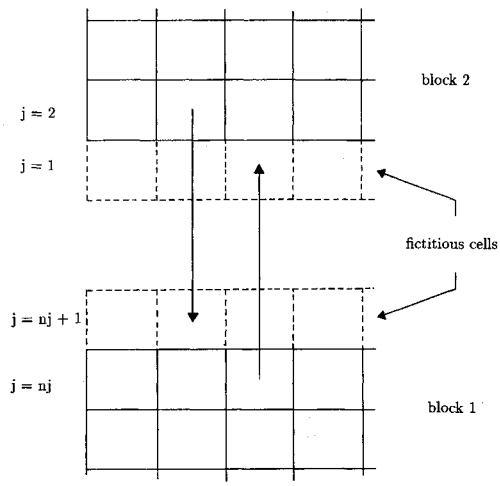

Fig. 1 Block interface treatment.

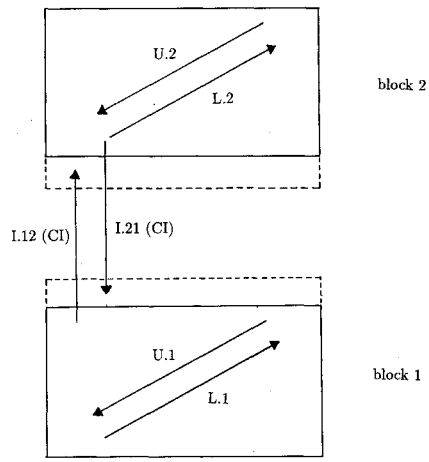

Fig. 2 Schematic diagram of synchronous (asynchronous) interface treatment.

1, the block matrix $B^-_{i,nj+1}$ of Eq. (27) is needed. According to the interface treatment, these two block matrices, that are function of variables exchanged between the blocks, are determined as

$$(B^+_{i,1})_{\text{block2}} = (B^+_{i,nj})_{\text{block1}} \quad \text{(phase I.12)} \tag{29}$$

$$(B^-_{i,nj+1})_{\text{block1}} = (B^-_{i,2})_{\text{block2}} \quad \text{(phase I.21)} \tag{30}$$

Due to the sequential character of the synchronous interface treatment, the blocks are strongly coupled.

The asynchronous-interface approach amounts to perform independently the forward and backward sweeps on each block with an explicit interface treatment. Hence, referring to Fig. 2, phases L.1, U.1, and L.2, U.2 are performed simultaneously. Then, once the solution is obtained at all interior cells of the two blocks, it is cross-injected for interface treatment (phase CI) as done in the I phase of the synchronous approach [Eqs. (29) and (30)]. In this approach the two blocks are more loosely coupled. However, the approach has the potential for parallel applications. Indeed, the execution of the tasks for the different blocks can be simultaneously dispatched to different processors, and then, by message-passing procedure, cross injection can be performed.

Bleed System Simulation

In the present work we are concerned only with the effects of bleed rather than with the details of the flow through the bleed passages. Therefore, appropriate boundary conditions must be imposed to account for these effects. The boundary-layer control system is simulated by assuming that the flow

through the bleeding passages is driven by the pressure difference between the (shock) downstream pressure and the pressure inside the passages. Consequently, at the bleeding boundary the pressure is imposed, and the entropy, the normal Riemann invariant, and the tangential velocity component are extrapolated in the direction normal to the boundary.

Results

Supersonic and hypersonic inlet flows have been computed to assess the validity of the present finite-volume multiblock approach and its ability to account for a boundary-layer control system. Freestream boundary conditions are imposed at inflow, no-slip and fixed wall temperature conditions are enforced along the centerbody and cowl surfaces, and second-order extrapolation conditions are set at the outflow boundaries.

NASA P8 Hypersonic Inlet

The first test case has been selected for validation purposes. The NASA P8 represents a typical configuration of a hypersonic air-breathing vehicle inlet with high contraction ratio and mixed-type compression, designed to provide an internal throat compression ratio $\beta_c = 8$. The numerical solution has been obtained by using two blocks of 176 × 48 and 176 × 14 cells with the normal mesh spacing $\Delta y/L$ (where L is the height of the inlet entrance section) ranging from 0.2×10^{-3} to 0.5×10^{-1}, corresponding to viscous coordinates (y^+) varying from 35 at the wedge leading edge to approximately 5 near the throat, and an aspect ratio of about 240 in the proximity of the wall. Approximately 20 cells (at the throat section) are fitted within the centerbody and cowl boundary layers.

For this test case both the synchronous and asynchronous block-interface treatments have been tested. The computed results show no differences, and only those obtained with the asynchronous approach are reported. For high Mach number flows the robustness of the scheme is affected by the selected values of the Courant-Fredrichs-Lewy (CFL) number, the parameters r_A and r_B (that determine the diagonal dominance of the implicit operator), and often by the Jacobian matrices that are evaluated.[6,7] In the present applications, the computations have been performed with a CFL number equal to 2, the Jacobian matrices have been reevaluated every two cycles, and the parameters r_A, r_B have been set equal to 1.6. For this test case the entropy factor δ has been set equal to 0.425 (by numerical experiments it has been found that smaller values do not yield stable solutions).

Experimental tests have been conducted in the NASA Ames 3.5-ft hypersonic wind tunnel[12] at a nominal freestream Mach number $M_\infty = 7.4$ and unit Reynolds number $Re_\infty = 8.86 \times 10^6 \text{m}^{-1}$. The freestream total pressure and temperature are, respectively, $p_\infty^0 = 4.14 \times 10^6$ Pa and $T_\infty^0 = 811$ K, and the wall temperature is $T_{\text{wall}} = 303$ K. The forebody wedge angle is $\theta = 6.5$ deg, that yields a design Mach number of 6.032 at the inlet entrance. This inlet configuration is such that the cowl-generated shock wave should cancel at the centerbody, to provide a uniform flow at the throat. Real gas effects are neglected due to the rather low temperature values, and the flow is assumed to be fully turbulent.

Iso-Mach lines are shown in Fig. 3. The shock wave that is generated at the wedge leading edge (that in an inviscid simulation hits the cowl leading edge[2]) crosses the interface between the two blocks ahead of the cowl leading edge, thus allowing for flow spillage. The shock wave generated at the cowl lip reflects on the centerbody and interacts with the boundary layer, thus causing a nearly separated flow. The relatively thick boundary layer is clearly observed in the contour plots. Compression waves are generated by the continuous curvature of the internal cowl surface and are clearly shown in the iso-pressure contours of Fig. 4. The centerbody and cowl pressure p/p_∞ vs x/L are plotted in Figs. 5 and 6. Having neglected the three-dimensional effects, the pressure

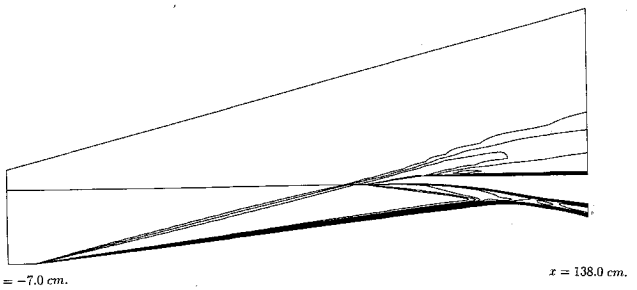

Fig. 3 Iso-Mach lines ($\Delta M = 0.50$) for NASA P8 hypersonic inlet.

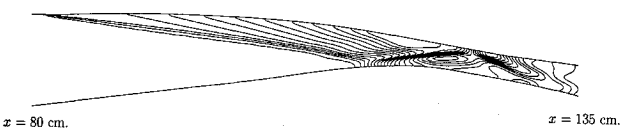

Fig. 4 Iso-pressure lines ($\Delta p = 1.75$) for NASA P8 hypersonic inlet.

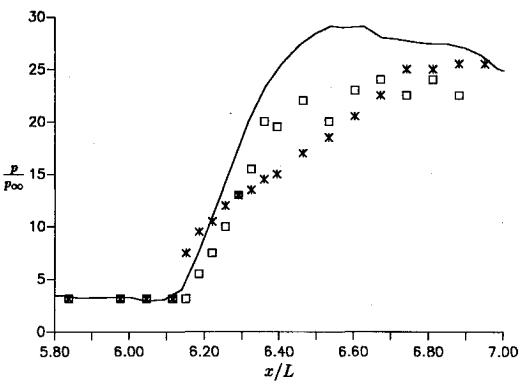

Fig. 5 Centerbody pressure p/p_∞ vs x/L for NASA P8 hypersonic inlet (—, present method; □, experimental[12]; *, design[12]).

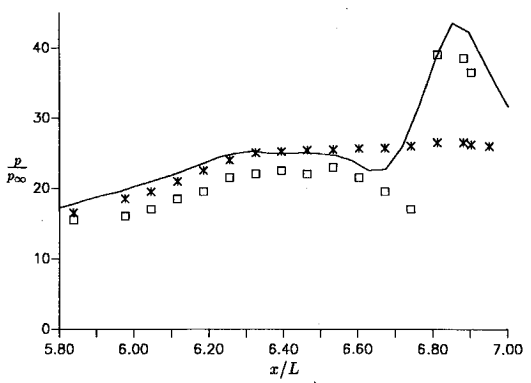

Fig. 6 Cowl pressure p/p_∞ vs x/L for NASA P8 hypersonic inlet (—, present method; □, experimental[12]; *, design[12]).

level is overpredicted with respect to the experiments[12] (about 20% on the centerbody and 11% on the cowl, both at throat section). Along the cowl the numerical solution is in good agreement with the experiments. The design pressure value is constant in the region of the throat, and the cowl shock only partially cancels at the centerbody. The computed internal compression ratio is equal to $\beta_c = 9.957$, in disagreement with the design value of 8; however, it is in better agreement with the (estimated) measured value $\beta_c = 8.611$. The disagreement with respect to the design is due to the fact that the cowl-generated shock wave does not cancel at centerbody, but reflects strongly and affects the flow approaching the throat region. Computed results indicate that, due to the interaction between the cowl generated shock wave and the centerbody boundary layer, the flow nearly separates at $x/L \simeq 6.0$. However, this is not substantiated by the experiments due to the lack of information.

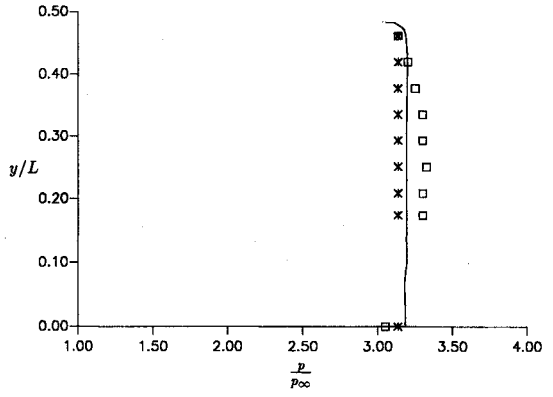

Fig. 7 Static pressure profile at inlet entrance section (—, present method; □, experimental[12]; *, design[12]).

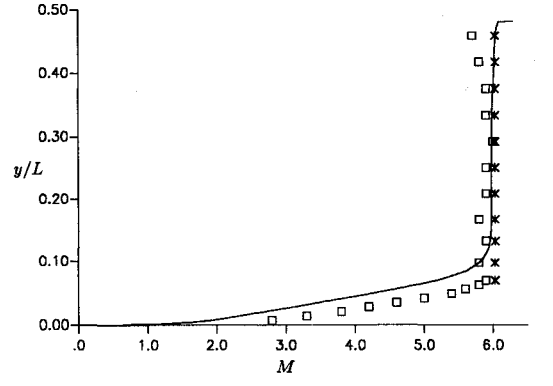

Fig. 8 Mach number profile at inlet entrance section (—, present method; □, experimental[12]; *, design[12]).

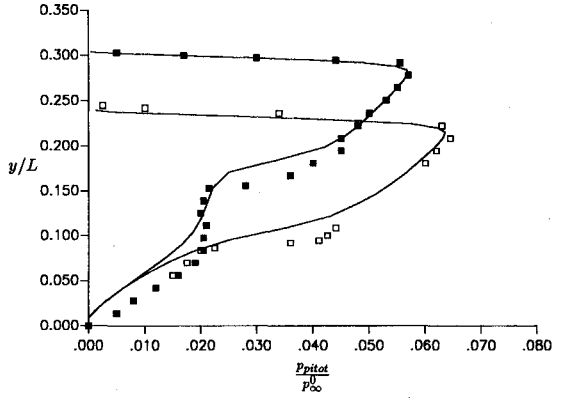

Fig. 9 Pitot pressure distributions at x = 104.14 cm (—, present method; ■, experimental[12]) and x = 109.22 cm (—, present method; □, experimental[12]).

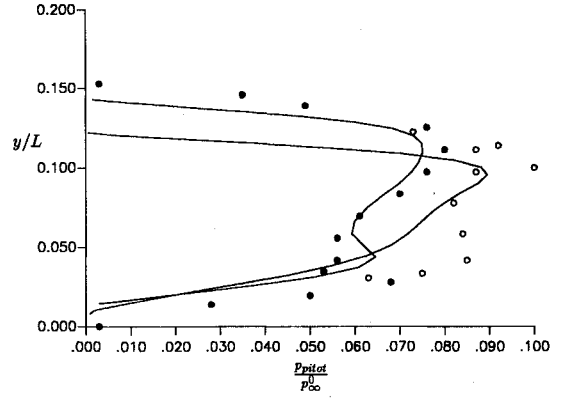

Fig. 10 Pitot pressure distributions at x = 116.84 cm (—, present method; ●, experimental[12]), and x = 125.73 cm. (—, present method; ○, experimental[12]).

Detailed comparisons of the computed and measured flow properties at the inlet entrance section (x = 81.28 cm) are shown in Figs. 7 and 8. The distributions of static pressure and Mach number agree well with the experiments. In Fig. 9 the Pitot pressure distributions at two-section upstream of the shock impingement (x = 104.14 cm and x = 109.22 cm) are reported, which are in good agreement with experiments, showing clearly the cowl-generated shock wave that crosses the sections. The pitot pressure profiles at x = 116.84 cm and x = 125.73 cm (throat section) are shown in Fig. 10. In the throat region the agreement with experiments becomes worse and this is due to the incorrect prediction of boundary-layer thickness. However, in the latter, the reflected shock at the cowl is observed. Figures 11–13 show the static pressure, the Mach number, and total temperature distributions at the throat section (x = 125.73 cm). The predicted static pressure is slightly higher than the experimental one (again due to the absence of three-dimensional effects). However, in the prox-

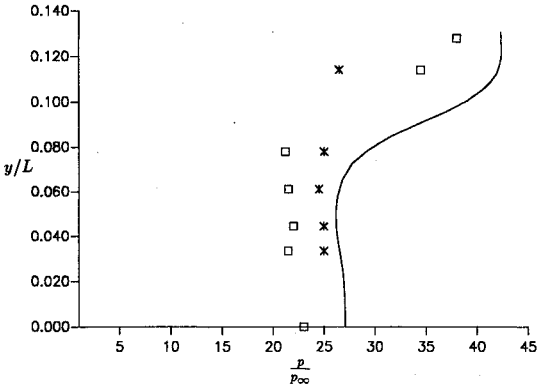

Fig. 11 Static pressure profile at inlet throat section (— present method; □, experimental[12]; *, design[12]).

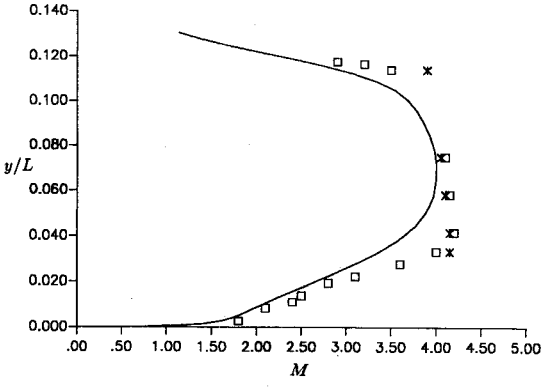

Fig. 12 Mach number profile at inlet throat section (—, present method; □, experimental[12]; *, design[12]).

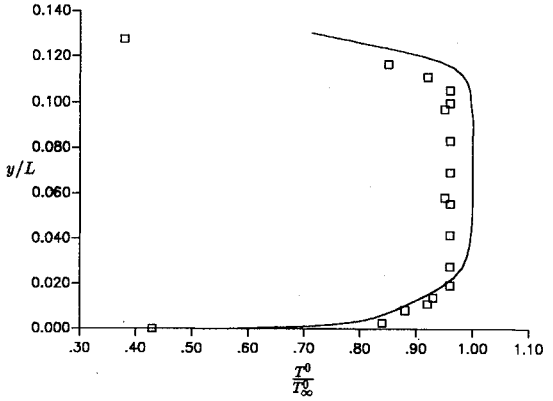

Fig. 13 Total temperature profile at inlet throat section (—, present method; □, experimental[12]).

imity of the centerbody a pressure value close to the design one is predicted. Very good agreement is shown for the Mach number and total temperature.

Supersonic Transport Inlet

The second test case corresponds to a mixed compression inlet of a supersonic aircraft of the new generation,[3] and it has been carried out to assess the ability of the model to simulate bleed, by assuming that along the centerbody there are three holes in communication with the ambient. The computed results are compared with those of Fujimoto et al.[3] The optimal cruise Mach number is $M_\infty = 2.5$, the flow is assumed to be laminar ($Re_\infty = 10^6$) and adiabatic. The computational domain has been partitioned into two blocks, with, respectively, 176 × 34 and 176 × 14 cells with the normal mesh spacing ranging from 0.1×10^{-2} to 0.7×10^{-1}, and an aspect ratio of about 42 near the wall. All computations have been performed with a CFL number equal to 5, and the Jacobian matrices have been re-evaluated every 2 cycles. The entropy function parameter (δ) is set equal to 0.125 for the solution without bleed; however, when the boundary-layer control system is active, it has been found necessary to increase this value to 0.425.

Figures 14–17 show the iso-density contour lives with and without bleeding and the sidewall and cowl pressure distribution vs x/L. When the boundary-layer control system is active, the freestream pressure in the bleed region is achieved. Moreover, a weak normal shock seems to appear immediately downstream of the bleed region. The pressure peak is the same with and without bleed, even though in the presence of bleed the shock pattern is displaced downstream. However, no effects on the outflow pressure arise. From the cowl pressure distribution, a normal shock at the throat is visible, and a higher peak pressure is predicted with bleed due to a stronger normal shock. Bleed through a third hole, which is located

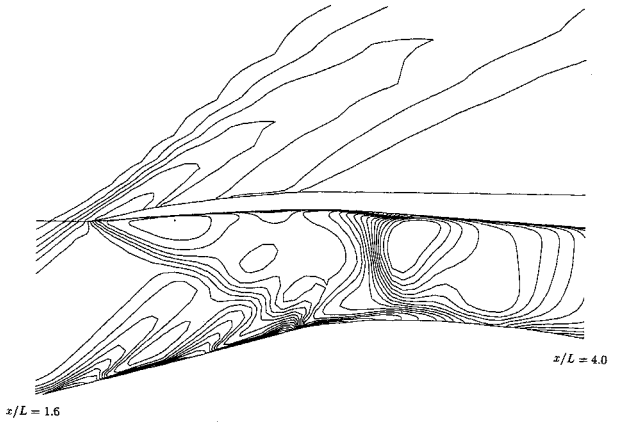

Fig. 14 Iso-density lines ($\Delta\rho = 0.15$) for supersonic transport inlet (bleeding).

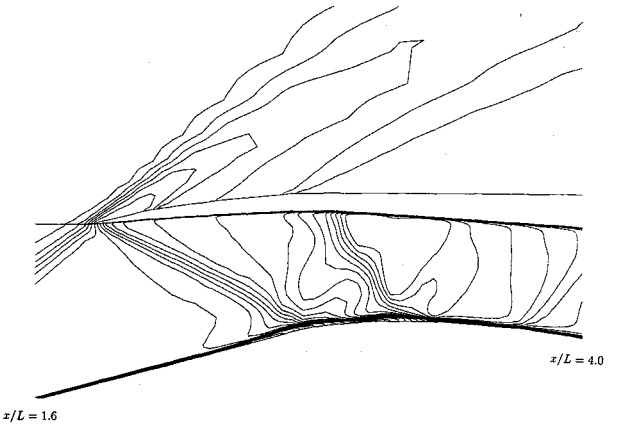

Fig. 15 Iso-density lines ($\Delta\rho = 0.15$) for supersonic transport inlet (no bleeding).

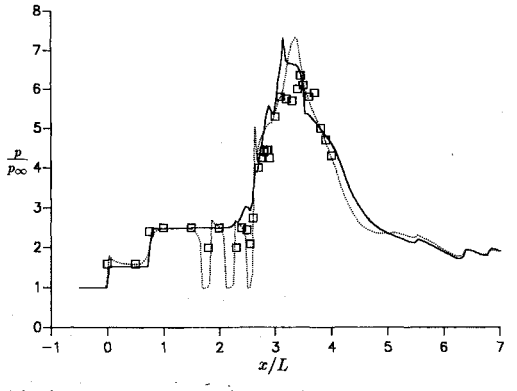

Fig. 16 Sidewall pressure p/p_∞ vs x/L for supersonic transport inlet (—, no bleeding, ···, bleeding; □, Ref. 3).

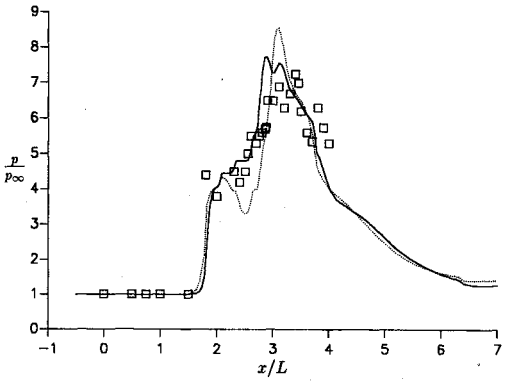

Fig. 17 Cowl pressure p/p_∞ vs x/L for supersonic transport inlet (—, no bleeding, ···, bleeding; □, Ref. 3).

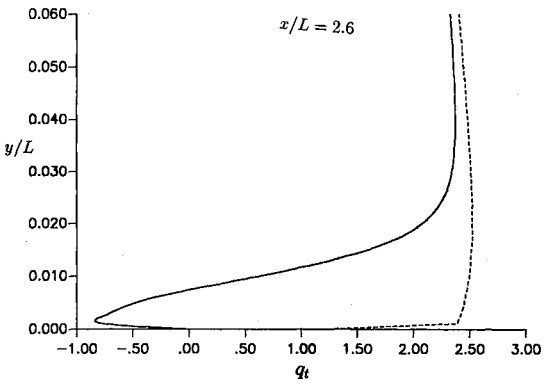

Fig. 18 Tangential velocity component through the third bleeding passage (—, no bleeding; ---, bleeding).

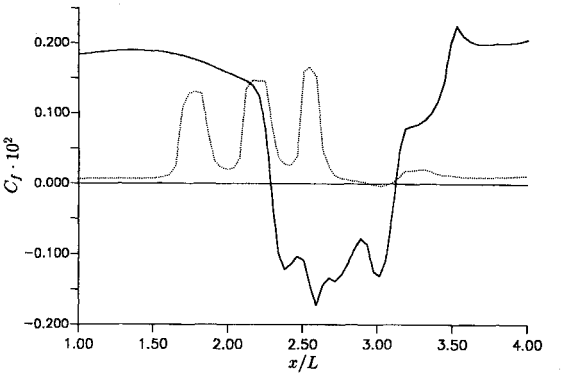

Fig. 19 Skin friction coefficient C_f vs x/L for supersonic transport inlet (—, no bleeding, ···, bleeding).

near the foot of the cowl lip-generated shock impinging on the centerbody boundary layer, affects the solution the most. In the absence of bleed, the flow recirculates due to the interaction of the latter shock with the boundary layer, as shown from the tangential velocity component (q_t) and skin friction distributions (see Figs. 18 and 19). When the bleed is active the entire boundary layer is sucked out, thus inhibiting the effects of the cowl-generated shock.

Conclusions

A multiblock finite-volume technique with a second-order total variation diminishing spatial discretization and an efficient implicit time integration has been developed to simulate complex internal flows at high Mach numbers. The method employs a lower and upper approximate factorization of the implicit operator with symmetric successive over relaxation sweeps. In the presence of multiblocks an asynchronous-interface treatment has been devised for an accurate coupling of the blocks.

A detailed validation by comparison of the computed results with experiments has shown the capabilities of the method to resolve complex high speed internal flows. The static pressure, Mach number, and total temperature distributions are well-predicted. The wall pressure levels are overpredicted, mainly due to the absence of three-dimensional effects, the fully turbulent assumption, and the intrinsic limitations of the algebraic turbulence model employed. However, the model is capable of predicting the effects of the contraction ratio and shock-wave boundary-layer interaction on the inlet performances. The model is also capable of simulating the influence of bleed (as a boundary-layer control system), whose effect is that of weakening the interaction of the cowl generated shock on the centerbody boundary layer.

References

[1]Knight, D. D., "Numerical Simulation of Realistic High-Speed Inlets Using the Navier-Stokes Equations," *AIAA Journal*, Vol. 15, No. 11, 1977, pp. 1583–1589.

[2]Garnero, P., "Ramjet Applications at Aérospatiale," *The Third Joint Europe/US Short Course in Hypersonics*, RWTH Aachen, Univ. of Technology, Aachen, Germany, Oct. 1990.

[3]Fujimoto, A., Niwa, N., and Sawada, K., "Numerical Investigation on Supersonic Inlet with Realistic Bleed and Bypass Systems," AIAA Paper 91-0127, Reno, NV, Jan. 1991.

[4]Jameson, A., and Yoon, S., "Lower-Upper Implicit Schemes with Multiple Grids for the Euler Equations," *AIAA Journal*, Vol. 25, No. 7, 1987, pp. 929–935.

[5]Rieger, H., and Jameson, A., "Solution of Steady Three-Dimensional Compressible Euler and Navier Stokes Equations by an Implicit LU Scheme," AIAA Paper 88-0619, Reno, NV, Jan. 1988.

[6]Grasso, F., and Marini, M., "LU Implicit TVD Scheme for the Solution of Viscous Two Dimensional High Speed Flows," AIAA Paper 91-1573, Honolulu, HI, June 1991.

[7]Grasso, F., and Marini, M., "LU Implicit TVD Scheme for the Solution of Viscous High Speed Flows," *AIAA Journal* (to be published).

[8]Baldwin, B. S., and Lomax, H., "Thin Layer Approximation and Algebraic Model for Separated Turbulent Flows," AIAA Paper 78-0257, Huntsville, AL, Jan. 1978.

[9]Yee, H. C., Warming, R. F., and Harten, A., "Implicit TVD Schemes for Steady State Calculations," *Journal of Computational Physics*, Vol. 57, No. 3, 1985, pp. 327–360.

[10]Yee, H. C., Klopfer, G. H., and Montagnè, J. L., "High Resolution Shock Capturing Schemes for Inviscid and Viscous Hypersonic Flows," NASA TM 100097, April 1988.

[11]Bassi, F., Grasso, F., and Savini, M., "Finite Volume TVD Runge-Kutta Scheme for Navier Stokes Computations," *Lecture Notes in Physics*, Springer-Verlag, Berlin, Vol. 323, 1989, pp. 131–136.

[12]Gnos, A. V., Watson, E. C., Seebaugh, W. R., Sanator, R. J., and DeCarlo, J. P., "Investigation of Flow Fields Within Large-Scale Hypersonic Inlet Models," NASA TN D-7150, April 1973.